International Journal of Heat and Fluid Flow 29 (2008) 626–639

Contents lists available at ScienceDirect

International Journal of Heat and Fluid Flow

journal homepage: www.elsevier.com/locate/ijhff

Implicit LES applied to zero-pressure-gradient and adverse-pressure-gradient boundary-layer turbulence

S. Hickel *, N.A. Adams

Institute of Aerodynamics, Technische Universität München, 85747 Garching, Germany

ARTICLE INFO

Article history:
Received 9 November 2007
Received in revised form 5 March 2008
Accepted 8 March 2008
Available online 16 May 2008

Keywords:
Large-eddy simulation
Subgrid-scale modeling
Boundary layer
Transition
Separation

ABSTRACT

Further development of large-eddy simulation (LES) faces as major obstacles the strong coupling between subgrid-scale (SGS) modeling and the truncation error of the numerical discretization. One can exploit this link by developing discretization methods where the truncation error itself functions as an implicit SGS model. The adaptive local deconvolution method (ALDM) is an approach to LES of turbulent flows that represents a full coupling of SGS model and discretization scheme. To provide evidence for the validity of this new SGS model, well resolved large-eddy simulations of a fully turbulent flat-plate boundary-layer flow subjected to a constant adverse pressure gradient are conducted. Flow parameters are adapted to an available experiment. The Reynolds number based on the local free-stream velocity and momentum thickness is 670 at the inflow and 5100 at the separation point. Clauser's pressure-gradient parameter increases monotonically from 0 up to approximately 100 since a constant pressure gradient is prescribed. The adverse pressure gradient leads to a highly unsteady and massive separation of the boundary layer. The numerical predictions agree well with theory and experimental data.

1. Introduction

Large-eddy simulation (LES) is becoming a more and more widely used simulation tool for the time-accurate prediction of unsteady flows at high Reynolds numbers. With LES the Navier–Stokes equations are numerically solved on a grid that is too coarse to resolve all scales representing the turbulent fluid motion. The unavailable small-scale information, however, is crucial for the proper evolution of large-scale structures in the flow. Therefore, the *effect* on the resolved scales of their non-linear interactions with the unresolved subgrid-scales (SGS) has to be represented by an SGS model.

The subgrid-scale model of a large-eddy simulation generally operates on flow scales that are marginally resolved by the underlying discretization scheme. Consequently, the discretization and the SGS model are linked. One can exploit this link by developing discretization methods where the truncation error itself functions as implicit SGS model. Approaches where SGS model and numerical discretization are merged are called implicit LES, refer to Grinstein et al. (2007) for an introduction. Employing implicit LES for prediction requires numerical methods that are specially designed, optimized, and validated for the particular differential equation to be solved (Domaradzki and Radhakrishnan, 2005). A full coupling of SGS model and discretization scheme cannot be achieved without incorporating physical reasoning into the design of the implicit SGS model.

Representing a full merger of discretization and SGS model, the adaptive local deconvolution method (ALDM) has the potential to be a reliable, accurate, and efficient method for LES of incompressible Navier–Stokes turbulence (Hickel et al., 2006). The implicit SGS model provided by this discretization can be interpreted as a combination of eddy-viscosity and scale similarity modeling. Model parameters were determined by a spectral-space analysis of the effective eddy viscosity in isotropic turbulence in the Reynolds number's infinite limit. Implicit large-eddy simulation was made rigorous by constraining the numerical dissipation to the physical SGS dissipation obtained from the analysis of non-linear interactions in turbulence. The good performance of the implicit model is demonstrated for canonical configurations, e.g., three-dimensional homogeneous isotropic turbulence (Hickel et al., 2006) and plane channel flow (Hickel and Adams, 2007). Predictions of ALDM agree well with theory and experimental data. It was demonstrated that the implicit SGS model performs at least as well as established explicit models.

The objective of the present paper is to prove the validity of the ALDM approach for a far more complex flow configuration. A numerical investigation of an incompressible fully turbulent flat-plate boundary-layer flow subjected to a constant adverse pressure gradient (APG) is carried out. Reynolds number and pressure-gradient parameters are adapted to the experimental setup of Inding-er et al. (2006) who conducted measurements in a closed-circuit

* Corresponding author.
E-mail address: sh@tum.de (S. Hickel).

0142-727X/$ - see front matter © 2008 Elsevier Inc. All rights reserved.
doi:10.1016/j.ijheatfluidflow.2008.03.008

water tunnel. Under the conditions considered here the adverse pressure gradient leads to a highly unsteady and massive separation. Neither separation nor reattachment are fixed in space. Showing a strongly irregular shape, the instantaneous separation line has spanwise and temporal excursions that are significantly larger than the mean boundary-layer thickness.

The applicability constraints of available turbulence models are well known for pressure-induced boundary-layer separation. Direct numerical simulations provide high accuracy but are limited to low Reynolds number and moderate flow complexity. A frequently cited study is that of Na and Moin (1998a,b) where the turbulence is barely developed. Spalart and Coleman (1997) performed DNS of weakly separated boundary-layer flows. Manhart and Friedrich (2002) presented DNS of weak separation adapted to the experiment by Kalter and Fernholz (2001), where Reynolds number of the DNS is half of the experimental one.

To our knowledge, this work represents the first successful reproduction of an experiment of massively separated flat-plate boundary-layer flow by LES. The Reynolds number based on the local free-stream velocity and momentum thickness is $Re_{\delta_2} = 670$ at the inflow and $Re_{\delta_2} = 5100$ at the separation point. Clauser's pressure-gradient parameter increases monotonically from $\beta = 0$ up to around $\beta = 100$ since a constant pressure gradient is prescribed corresponding to the reference experiment.

This paper is structured as follows: First, the reference experiment of Indinger is introduced in Section 2. Our numerical method is described in Section 3. Then an LES of laminar-turbulent transition in a zero-pressure-gradient boundary layer is presented in Section 4 to demonstrate the validity of this methodology. The computational setup and results for the adverse-pressure-gradient boundary-layer flow are discussed in Sections 5 and 6, respectively.

2. Reference experiment

Recently Indinger et al. (2004, 2006) have presented measurements for a fully turbulent flat-plate boundary layer with a constant APG. Fig. 1 shows the experimental setup in the test section of a closed-circuit water tunnel with flow from left to right. The measurements were conducted in the boundary layer developing on an inclined flat plate. A flexible curved wall on the opposite side is used to generate a pressure gradient, where the pressure-gradient parameters can be controlled by adjusting the curvature. The flat plate, inclined by 4°, has an overall length of 0.725 m, and a flap at the end prevents trailing-edge separation. The plate surface is made from mirrored glass, which facilitates optical measurements close to the wall. Several auxiliary devices are necessary to control the flow quality. A bypass system below the flat plate and a suction system have been installed to control the stagnation-point flow at the elliptic leading edge of the plate. To prevent boundary-layer separation at the opposite wall due to curvature effects, a second suction system consisting of three slots is installed at the upper rear end of the test section. For a detailed description of the experimental facilities refer to Indinger (2005).

In the spanwise center plane, the static wall pressure and profiles of the streamwise velocity component were measured using pressure taps and a one-component LASER Doppler anemometry (LDA) system, respectively. For measurements of the wall shear stress, a Preston tube was employed.

The available measurement data do not provide the fully 3-D statistics that are essential for an analysis of the turbulent non-equilibrium flow. To gain a deeper understanding of wall-bounded turbulence in the vicinity of massive pressure-induced separation a numerical investigation by LES was carried out and is reported in the following.

3. Numerical method

The flow is described by the incompressible Navier–Stokes equations. The equations are discretized by a fractional step method on a staggered Cartesian mesh. For time advancement the explicit third-order Runge–Kutta scheme of Shu (1988) is used. The time-step is dynamically adapted to satisfy a Courant–Friedrichs–Lewy condition with CFL = 1.0. The spatial discretization is based on the finite-volume method. Second-order centered schemes are used for discretizing the pressure-Poisson equation and diffusive terms. The Poisson solver employs fast Fourier transforms in the spanwise direction and the stabilized bi-conjugate gradient (BiCGstab) method (van der Vorst, 1992) in the streamwise and wall-normal directions. The Poisson equation is solved at every Runge–Kutta substep. The convective terms are treated by ALDM which represents a full merging of numerical discretization and SGS model. With ALDM, a local reconstruction of the unfiltered

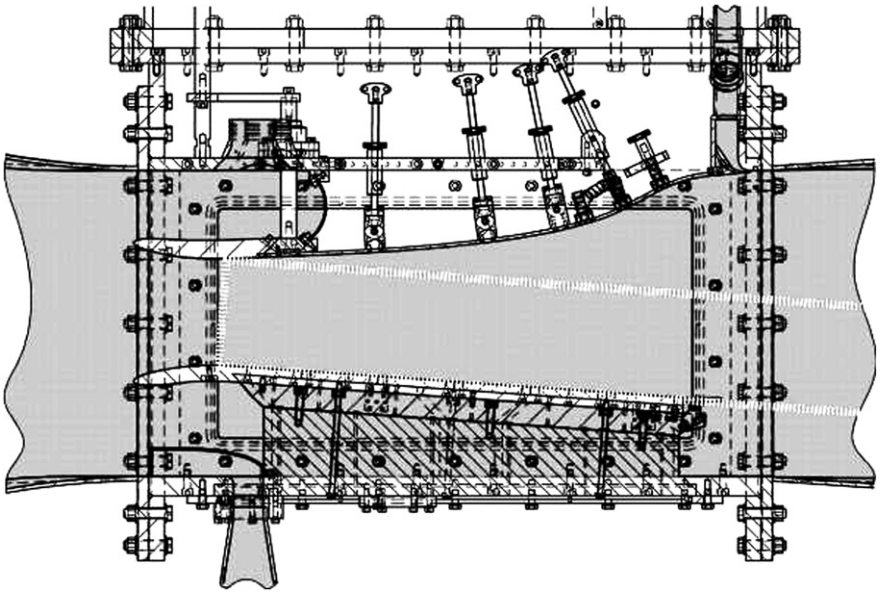

Fig. 1. Experimental setup in the test section of a water tunnel (Indinger et al., 2004). The computational domain of the present LES is marked by the dashed white line.

solution is obtained from a solution-adaptive combination of Harten-type deconvolution polynomials. Deconvolution is regularized by limiting the degree k of local approximation polynomials to $k \leqslant K$ and by permitting all polynomials of degree $1 \leqslant k \leqslant K$ to contribute to the reconstructed solution. Adaptivity of the deconvolution operator is achieved by dynamically weighing the respective contributions. A numerical flux function operates on the approximately deconvolved solution. The solution-adaptive stencil-selection scheme and the numerical flux function contain free model parameters that have been calibrated for canonical inertial-range turbulence (Hickel et al., 2006). These parameters remained unchanged for all subsequent applications. The results presented in this paper are obtained by the SALD method (Hickel and Adams, 2006) that represents an implementation of ALDM with improved computational efficiency. The validity of this numerical methodology has been established for plane channel flow (Hickel and Adams, 2007), for separated channel flow (Hickel et al., in press), and for passive scalar mixing (Hickel et al., 2007).

4. Validation for zero-pressure-gradient turbulent boundary-layer flow

A suitable test scenario for validation of the numerical method for boundary-layer flows is a zero-pressure-gradient (ZPG) boundary layer, where many analytical and computational data are available for reference. The intuitive approach would be to simulate the spatial development of a boundary layer using an extensive computational domain. A popular alternative represents temporal boundary-layer simulation, where the spatial evolution is modeled by the temporal evolution in a thin computational box moving with the flow. The temporal approach requires only a fraction of the computational time of a spatial simulation. The transfer of numerical results from the temporal to the spatial description is limited due to effects of the finite domain size and the boundary conditions. These differences are important in laminar-turbulent transition studies, but the effect on many integral quantities, such as mean velocity profile and skin friction coefficient, is small.

Table 1
Cell sizes in inner and outer coordinates for temporal LES of zero-pressure-gradient turbulent boundary-layer flow

Re_{δ_2}	h_x/l^+	$h_y/l^+\|_{wall}$	h_z/l^+	h_x/δ	$h_y/\delta\|_{wall}$	h_z/δ
120	37.6	1.80	18.8	0.58	0.027	0.29
670	28.8	1.38	14.4	0.10	0.0048	0.05
1410	26.2	1.26	13.1	0.046	0.0022	0.023

We perform a temporal simulation of ZPG boundary-layer flow in a double-periodic computational domain. The flow is initialized to a laminar Blasius boundary-layer profile with thickness δ and free-stream velocity U_∞, superposed with low-amplitude white-noise fluctuations. This initial disturbance is expected to grow during the simulation and eventually leads to transition of the flow to a turbulent state. The computational box has the extents $48\delta \times 124\delta \times 128\delta$ in streamwise $\times$ wall-normal $\times$ spanwise directions, respectively. A no-slip condition is imposed at the wall and the free-stream interface is modeled by the decay condition, see Section 5.2. Periodic boundary conditions are imposed in streamwise and spanwise direction. The computational domain is discretized with $48 \times 96 \times 256$ cells. Hyperbolic grid stretching is applied in the wall-normal direction in such a way that the initial boundary-layer thickness is resolved by 15 cells. Note that for a given grid the effective resolution improves as the boundary-layer thickness increases during the simulation. Table 1 summarizes grid parameters in outer and inner scaling at three instants. The initial Reynolds number is $Re_{\delta_1} = 300$, which corresponds to $Re_{\delta_2} \approx 120$, where

$$Re_{\delta_1} = \frac{U_\infty \delta_1}{\nu} \tag{1}$$

is the Reynolds number based on U_∞, the kinematic viscosity ν and the displacement thickness δ_1, see Eq. (12), and

$$Re_{\delta_2} = \frac{U_\infty \delta_2}{\nu} \tag{2}$$

is the Reynolds number based on the momentum thickness δ_2, see Eq. (13).

Laminar-turbulent transition is one of the most demanding test cases for LES. When white noise is used, most energy is injected into decaying modes and only a low percentage of the disturbance excites the instability modes of the laminar flow. For the onset of transition the SGS model must not affect the growth and amplification of these unstable modes. Most eddy-viscosity SGS models do not satisfy this requirement without ad hoc modifications.

The large spanwise extent of the computational domain was chosen to improve the accuracy of turbulence statistics that are computed from instantaneous snapshots by spatial averaging. Fig. 2a shows the evolution of the dimensionless friction coefficient

$$C_f = \frac{2U_\tau^2}{U_\infty^2} \tag{3}$$

for a temporal LES using ALDM, where the wall-friction velocity $U_\tau = \sqrt{\nu|\langle\partial_y u\rangle|_{wall}}$ is the characteristic velocity scale close to the

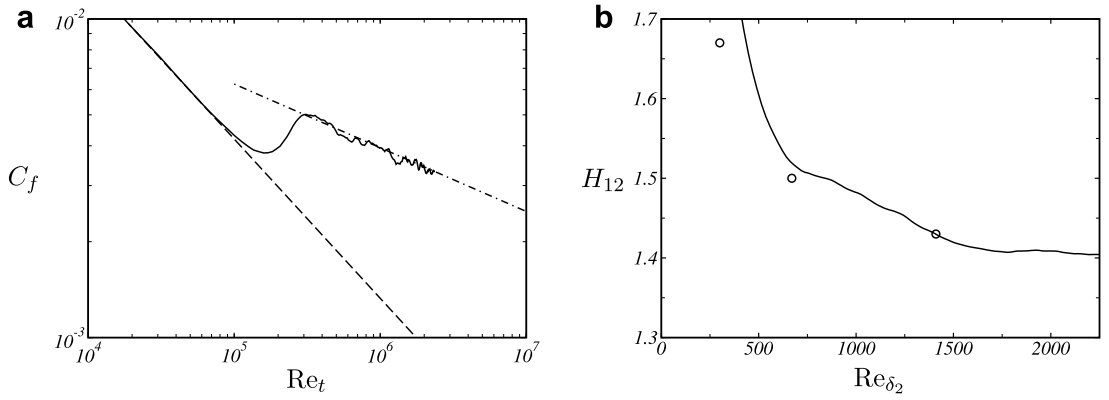

Fig. 2. (a) Evolution of friction coefficient C_f in temporal LES of ZPG flow. — present LES, - - - - laminar theory $C_f \sim (Re_t)^{-1/2}$, ·-·-· turbulent theory $C_f \sim (Re_t)^{-1/5}$. (b) Evolution of the shape factor H_{12}. — present LES, ◦ DNS (Spalart, 1988).

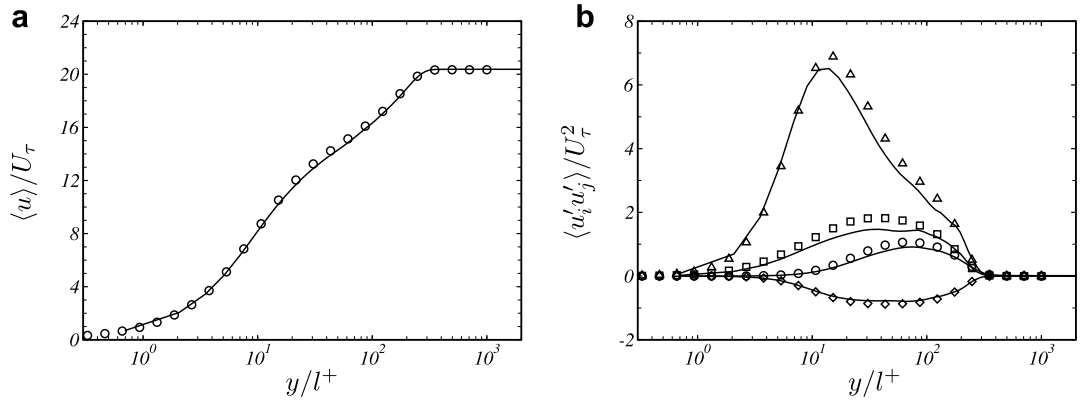

Fig. 3. Profiles of mean velocity and Reynolds stresses for turbulent ZPG boundary layer flow at $Re_{\delta_2} = 670$. — present LES, symbols denote reference DNS (Spalart, 1988).

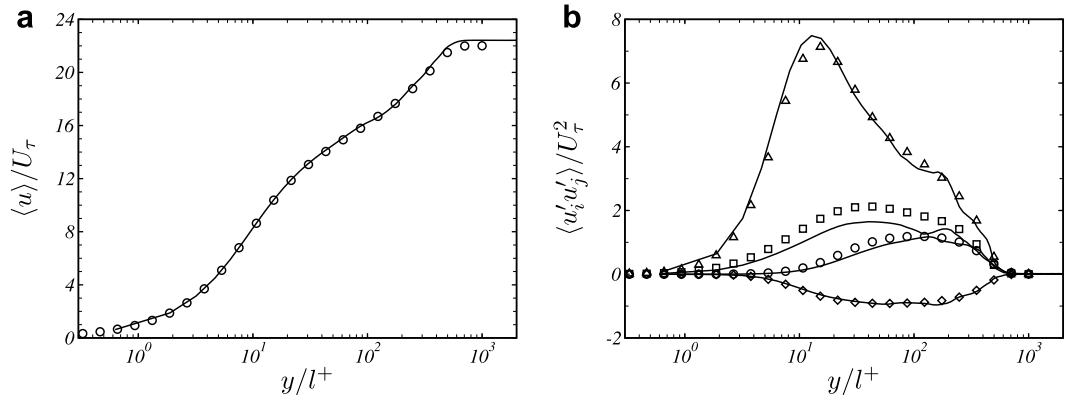

Fig. 4. Profiles of mean velocity and Reynolds stresses for turbulent ZPG boundary layer flow at $Re_{\delta_2} = 1410$. — present LES, symbols denote reference DNS (Spalart, 1988).

wall. During the growth of the laminar boundary layer the friction coefficient follows the theoretical solution:

$$C_f \sim (Re_t)^{-1/2}, \tag{4}$$

where the Reynolds number is defined as

$$Re_t = \frac{tU_\infty^2}{\nu}. \tag{5}$$

One can clearly see that the boundary layer undergoes laminar-turbulent transition. Eventually the friction coefficient follows the turbulent law:

$$C_f \sim (Re_t)^{-1/5}. \tag{6}$$

The evolution of the shape factor $H_{12} = \delta_1/\delta_2$ as a function of the momentum thickness Reynolds number Re_{δ_2} is shown in Fig. 2b. The prediction of our temporal LES with ALDM is in good agreement with DNS by Spalart (1988) in the later turbulent stages. Results from LES and DNS do not match for the low Reynolds number $Re_{\delta_1} = 500$ ($Re_{\delta_2} \approx 300$). Spalart's DNS gives turbulent velocity profiles that can hardly be obtained by natural transition at this small Reynolds number. Note that the critical Reynolds number for linear stability theory of a Blasius profile is $Re_{\delta_1} = 520$ (Schlichting, 1979). In order to remedy this disagreement, Spalart proposed to distinguish between *developed* turbulence and *sustained* turbulence and argued that boundary-layer turbulence cannot be fully developed at Reynolds number lower than $Re_{\delta_2} = 600$, but the turbulence, once imposed, can be sustained in the simulations at much lower Reynolds numbers.

In the turbulent regime the performance of the implicit SGS model is evaluated by comparing profiles of mean velocity and Reynolds stresses with DNS data. Figs. 3 and 4 show results for the mean velocity profile and Reynolds stresses from LES and DNS at $Re_{\delta_2} = 670$ and at $Re_{\delta_2} = 1410$, respectively. All data is normalized with the friction velocity U_τ and the viscous length scale $l^+ = \nu/U_\tau$. ALDM apparently predicts the anisotropic turbulence statistics correctly. Characteristic boundary-layer parameters are given in Table 2.

Table 2
Characteristic parameters of the temporal boundary-layer simulations

		Re_{δ_2}	Re_{δ_1}	$C_f \times 10^3$	H_{12}	H_{32}
First station	Reference	670	1000	4.8	1.49	n/a
	Present	662.8	1008.0	4.79	1.52	1.74
Second station	Reference	1410	2000	4.2	1.42	n/a
	Present	1419.9	2028.3	4.07	1.43	1.76

5. Computational setup for adverse-pressure-gradient turbulent boundary-layer flow

5.1. Computational domain

The computational domain considered in the LES is indicated by a dashed white line in Fig. 1. It has an overall physical length of 1.01 m. The spanwise and wall-normal extents are 0.036 m and 0.15 m, respectively. For comparison, the displacement thickness of the inflow boundary layer is $\delta^*(x = 0) = 0.0008$ m. In the following all data is made dimensionless with reference length 1 meter and reference velocity 1 meter per second, i.e., all measures are given in SI units. Indinger (2005) provides reference measurement

data for the attached APG flow up to the streamwise coordinate $x = 0.4$, where the boundary layer separates only intermittently. However, numerical results for the separated flow can be evaluated indirectly through the correct reproduction of the separation's upstream effect. In order to minimize the effect of the outflow boundary condition, the computational domain has been chosen in such a way that the massively separated flow zone is covered entirely.

The Cartesian grid consists of $2038 \times 144 \times 144$ finite volumes. The spacing is homogeneous in streamwise and in spanwise directions, where the cell dimensions are $h_x = 5 \times 10^{-4}$ and $h_z = 2.5 \times 10^{-4}$, respectively. In the wall-normal direction a hyperbolic stretching is used to increase resolution near the wall, resulting in the range of cell sizes $h_y = 2.4 \times 10^{-5}$ to $h_y = 1.0 \times 10^{-3}$. Cell sizes in inner variables, i.e. normalized by the viscous length scale l^+, are given in Table 3 for several downstream stations. The computational grid classifies the present LES as highly resolved. Grid parameters are chosen as to allow for a reliable simulation of the incoming ZPG boundary-layer flow.

5.2. Boundary conditions

The computational domain considered in the LES as indicated in Fig. 1 represents only a part of the experimental facility. The flow within the computational domain is determined by the surrounding flow which has to be represented by imposing appropriate boundary conditions. At the domain boundaries three layers of ghost cells are added so that stencils reaching beyond the domain boundary can be used. The methods employed for assigning data to these ghost cells are described in the following.

Spanwise periodicity was imposed since the flow is supposed to be homogeneous in this direction. At the surface of the flat plate a no-slip condition $\bar{\boldsymbol{u}} = \boldsymbol{0}$ and a homogeneous Neumann condition for the pressure $\partial_y p = 0$ are imposed. The viscous sublayer is resolved and no wall model is used. The ghost cells are filled with the analytical solution for Stokes flow as recommended by Morinishi et al. (1998).

The free-stream interface is modeled by prescribing a Dirichlet condition for the pressure $p = p_{fs}(x,t)$. The velocity is locally split into the instantaneous spanwise mean

$$\bar{\boldsymbol{u}}_{\text{mean}} = \frac{\int \bar{\boldsymbol{u}} \mathrm{d}z}{\int 1 \mathrm{d}z}$$

and local instantaneous fluctuations

$$\bar{\boldsymbol{u}}_{\text{fluc}} = \bar{\boldsymbol{u}} - \bar{\boldsymbol{u}}_{\text{mean}}.$$

Mean velocity and fluctuations are extrapolated from the computed domain to the ghost cells in such a manner that $\partial_y \bar{\boldsymbol{u}}_{\text{mean}} = \boldsymbol{0}$ and $\partial_y \bar{\boldsymbol{u}}_{\text{fluc}} = -\alpha \bar{\boldsymbol{u}}_{\text{fluc}}$ are fulfilled, respectively. The latter results in the decay condition $\bar{\boldsymbol{u}}_{\text{fluc}}(y) \propto \exp(-\alpha y)$. The value of the parameter $\alpha = 1/(4h_y)$ was determined from the wavelength of numerically induced oscillations that were observed when the decay condition was not used. This free-stream boundary condition allows for both outflow and inflow. Ghost cells are filled by using a discrete second-order approximation of the above equations.

Table 3
Grid parameters and averaging time in outer and inner time units

x	h_x/l^+	h_y/l^+	h_z/l^+	$t_{\text{ave}}U_\delta/\delta_1$	$t_{\text{ave}}U_\tau/l^+$
0.000	32.58	1.56–65.2	16.29	31755.6	85538.7
0.100	27.39	1.31–54.8	13.69	16950.9	60440.2
0.200	22.50	1.08–45.0	11.25	9404.9	40806.2
0.300	16.96	0.81–33.9	8.48	4806.4	23171.0
0.400	9.47	0.45–18.9	4.73	1952.5	7225.7
0.500	0.50	0.02–1.0	0.25	725.0	30.4
0.600	3.23	0.15–6.5	1.61	355.8	839.2

In the experiments, the pressure was measured at the plate surface only. For optimum agreement of the wall-pressure distribution with the experimental data, the free-stream pressure boundary condition for the present LES was reconstructed by a large number of low-resolution trial computations. The resulting free-stream pressure boundary condition is a function of the streamwise coordinate defined by

$$p_{fs}(x,t) = \rho \int_0^x (0.79 - 0.60x')\; b(x',t)\; \mathrm{d}x', \tag{7}$$

where ρ is the fluid's density. In the experimental facility, flow separation causes a break-down of the constant pressure gradient by its displacement effect. Therefore a positive pressure gradient should be imposed only within the zone of attached boundary-layer flow. In order to ensure smooth transients, we define

$$b(x,t) = \begin{cases} 0, & x < (x_B - x_{RB}) \\ 1 + \frac{x-x_B}{x_{RB}} - \frac{1}{2\pi}\sin(2\pi\frac{x-x_B}{x_{RB}}), & (x_B - x_{RB}) \leqslant x < x_B \\ 1, & x_B \leqslant x < x_E \\ 1 - \frac{x-x_E}{x_{RE}} + \frac{1}{2\pi}\sin(2\pi\frac{x-x_E}{x_{RE}}), & x_E \leqslant x < (x_E + x_{RE}) \\ 0, & (x_E + x_{RE}) \leqslant x \end{cases}. \tag{8}$$

Time dependency enters through $x_E = x_D(t) + 0.1$ where $x_D(t)$ is the instantaneous position of the spanwise averaged detachment line. A summary of all parameters is given in Table 4. The coefficients in the functionals (7) and (8) are determined in such a way that the mean pressure gradient at the wall matches the experiment.

At the inlet, fully turbulent inflow data is generated using a recycling technique, similar to that of Lund et al. (1998): Instantaneous turbulent structures are extracted at a downstream distance $l_{\text{rec}} \approx 40\delta^*$. Inside the boundary layer, target profiles for the fluctuating velocities are taken from Spalart's zero-pressure-gradient boundary-layer DNS (Spalart, 1988) at $Re_{\delta_2} = 670$. In the outer flow region, isotropic turbulence is assumed with a turbulence level of $Tu = 0.03$ matching the experiment. For the pressure a homogeneous Neumann condition $\partial_x p = 0$ is used.

Recycling techniques can sustain spurious oscillations with a wavelength proportional to the recycling length. In order to damp these oscillations the re-scaling factors are computed for each ghost-cell plane separately: For the innermost ghost-cell plane, target profiles are taken from the DNS of Spalart (1988). For the remaining two upstream planes, the target fluctuation profiles are damped in such a way that $\partial_x \langle \boldsymbol{u}'\boldsymbol{u}' \rangle = \langle \boldsymbol{u}'\boldsymbol{u}' \rangle / l_{\text{rec}}$ is satisfied.

At the outlet the ghost cells are filled by extrapolation. For a second-order centered discretization $\partial_x p = 0$ and $\partial_x^2 \boldsymbol{u} = \boldsymbol{0}$ are fulfilled. No artificial damping or sponge zone is used.

6. Results for adverse-pressure-gradient turbulent boundary-layer flow

For statistical analysis, the simulation was run for $t_{\text{ave}} = 23.7$ after reaching a stationary state. A clearer picture of the sample size is obtained from Table 3, where the averaging time expressed in typical boundary-layer time scales, i.e., $t_{\text{ave}}/(\delta^*/U_\infty)$ for the outer region and $t_{\text{ave}}/(l^+/U_\tau)$ near the wall. A typical timescale of the wall-turbulence, the ratio of turbulent kinetic energy to its produc-

Table 4
Parameters for the free-stream pressure boundary condition

Parameter		Value
x_B	Starting point of nominal pressure gradient	−0.025
x_{RB}	Length of starting ramp	0.02
x_E	End nominal pressure gradient	$x_D + 0.1$
x_{RE}	Length of end ramp	0.15
x_D	Location of spanwise averaged detachment line	Variable

tion rate, is about 15 wall time units l^+/U_τ (Spalart, 1988). The statistical analysis is conclusive for the attached flow up to $x \leqslant 0.475$. The separation bubble itself exhibits much larger time scale than the boundary-layer turbulence. From the available samples, fully converged results cannot be expected for higher-order statistics at locations within the separated zone.

6.1. Mean flow

A first impression of the investigated flow can be obtained from the mean streamlines in Fig. 5. Contour plots of the mean velocity solution are shown for the entire computational domain in Fig. 6. The influence of a strong adverse pressure gradient is evident. The mean-flow deceleration results in an increasing fraction of back-flow events and eventually causes strong boundary-layer separation. The boundary-layer separation is accompanied by a large wall-normal velocity component and intense interactions with the outer flow.

The mean static pressure imposed as a boundary condition at the free-stream interface is shown in Fig. 7. The mean pressure distribution at the wall is the non-linear response of the flow and strongly influenced by the boundary-layer separation. The oscillatory motion of detached flow regions has a significant effect on the upstream flow resulting in a deviation of the wall pressure from the imposed free-stream condition, see Fig. 7.

The resulting wall-pressure gradients $\langle \partial_x p \rangle_{\text{wall}}/\rho$ for LES and the experiment are shown in Fig. 8a. Taking into account the noise in derivatives computed from experimental data, LES results and experiment agree well. This first impression is confirmed by the observed deceleration of the free-steam velocity U_∞, see Fig. 8b, that can be measured more accurately. Mean-flow deceleration is directly caused by the APG through Bernoulli's equation and the excellent agreement of U_∞ confirms that the boundary conditions reproduce the experiment correctly.

Fig. 9 shows mean velocity profiles at six downstream stations that are representative for APG turbulent boundary-layer flow approaching separation. Also shown are available measurements. The data is not normalized in order to allow for a direct and unbiased comparison of experimental with numerical results. The mean velocity profiles of the present LES are in excellent agreement with the experiment.

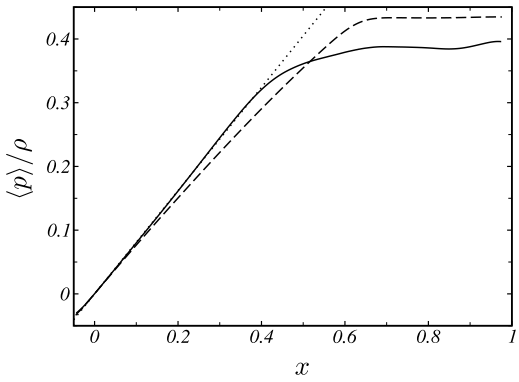

Fig. 7. Mean static pressure at the - - - - free-stream interface and at the — wall. The ····· dotted line denotes the target pressure gradient of 810 Pa/m according to experimental reference data.

6.2. Reverse flow parameter

The probability of back flow is quantified by the reverse-flow parameter

$$\chi = \frac{1}{2} - \frac{1}{2}\left\langle \frac{u}{|u|} \right\rangle \tag{9}$$

which measures the fraction of time that the flow moves upstream. Wall-normal profiles of χ are shown in Fig. 10 and streamwise profiles are shown in Fig. 11. We observe that flow separation is accompanied by the shift of the location of maximum χ away from the wall towards the detached shear layer.

In Fig. 10, the shape of the separation bubble is indicated by two lines that represent different criteria: The locations where the mean streamwise velocity component does vanish, i.e. $\langle u \rangle = 0$, and the locations where forward flow and upstream flow have

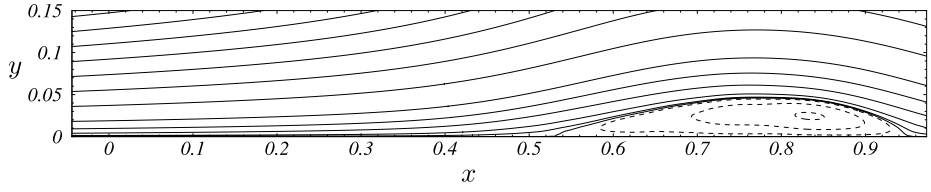

Fig. 5. Mean streamlines.

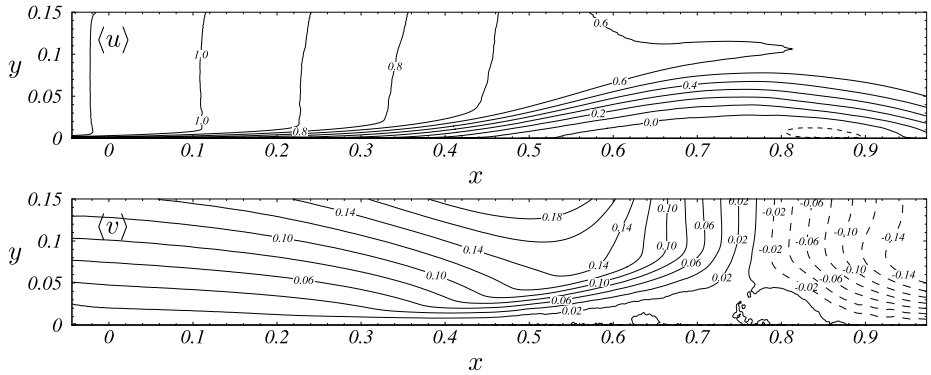

Fig. 6. Contours of mean velocity.

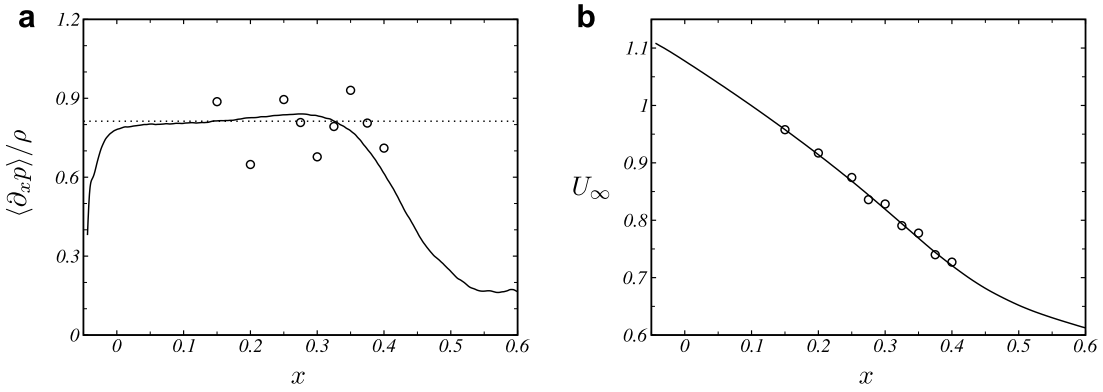

Fig. 8. (a) Mean pressure gradient at the wall, and (b) free-stream velocity at the boundary-layer edge for ○ experiment and — LES.

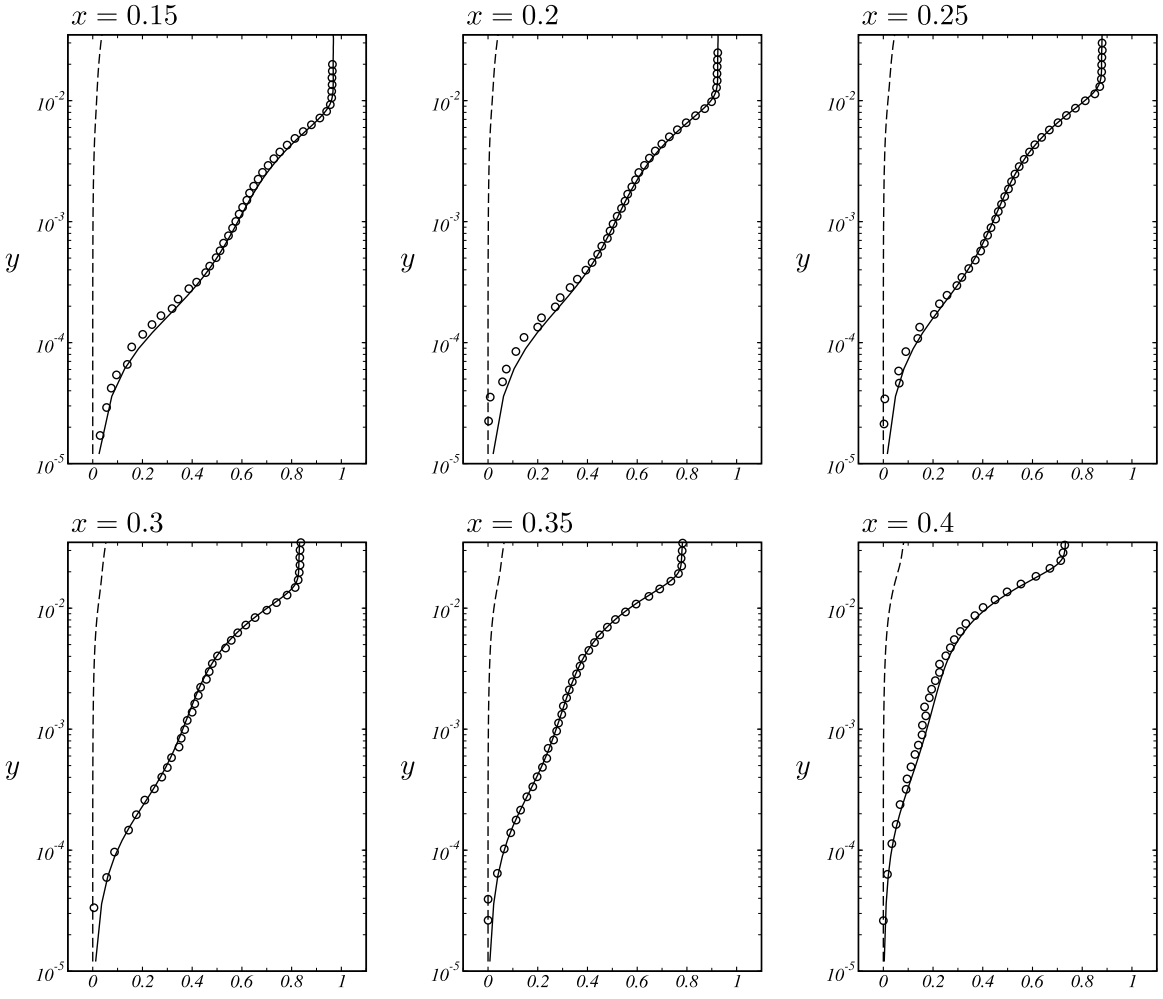

Fig. 9. Mean velocity profiles for several downstream stations. — $\langle u \rangle$ and - - - - - $\langle v \rangle$ for LES, ○ $\langle u \rangle$ for LDA.

equal probability ($\chi = 0.5$). Both criteria give a similar result, however, some differences can be observed close to the separation point: The wall-normal extent of the separated region is slightly larger for $\chi = 0.5$ than for $\langle u \rangle = 0$.

In order to define the separation state quantitatively, the following terminology has been proposed by Simpson (1981, 1989): *Incipient detachment* (ID) occurs with $\chi = 0.01$, *intermittent transitory detachment* (ITD) occurs with $\chi = 0.2$, *transitory detachment* (TD) occurs with $\chi = 0.5$, and *detachment* (D) occurs where the time-averaged wall shear stress is zero. The corresponding locations for the LES of the present configuration are given in Table 5. In agreement with most available data, our computational results confirm that TD and D occur at the same location.

6.3. Boundary-layer scales

A turbulent boundary layer can by characterized by several length scales. The boundary-layer thickness δ serves as a measure

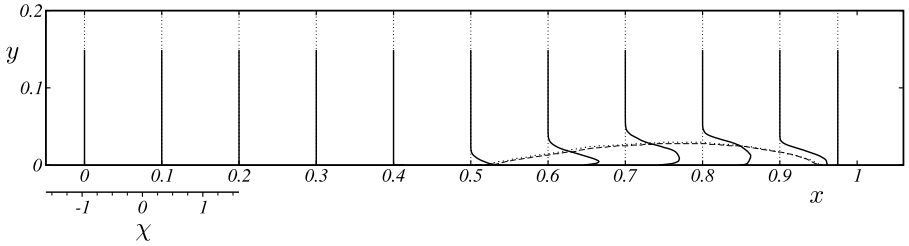

Fig. 10. Reverse-flow-parameter profiles at several downstream stations. — reverse-flow parameter, - - - - - $\langle u\rangle = 0$, ····· $\chi = 0.5$.

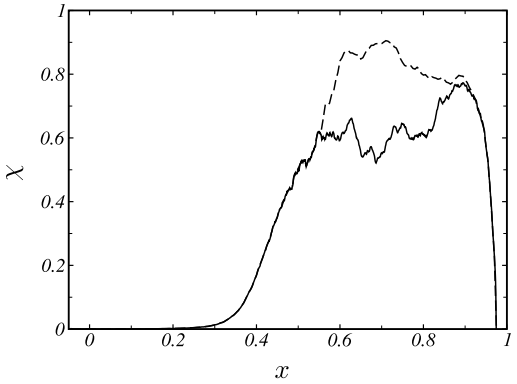

Fig. 11. Reverse-flow parameter: — at the wall and - - - - - maximum value.

Table 5
Separation state near the wall for present LES in Simpson's terminology

Term		Definition	Location
ID	Incipient detachment	$\chi = 0.01$	$x = 0.287$
ITD	Intermittent transitory detachment	$\chi = 0.2$	$x = 0.457$
TD	Transitory detachment	$\chi = 0.5$	$x = 0.502$
D	Detachment	$\langle\tau_w\rangle = 0$	$x = 0.502$

for the largest structures in the boundary-layer flow. It is defined as the distance away from the wall where 99 percent (δ_{99}) of the free-stream velocity U_∞ is reached. In APG boundary-layer flow, however, the velocity is not constant in the free stream. For the experimental data, Indinger (2005) has manually selected the LDA measurement points representing the transition region between boundary layer and free stream. For the LES, the boundary-layer edge is determined as the point where the streamwise velocity starts to diverge from the linear dependency on wall distance of the external flow. The velocity at this point is defined as U_∞ and δ follows from

$$\delta = y(\langle u\rangle = U_\delta) \tag{10}$$

with

$$U_\delta = 0.99\ U_\infty. \tag{11}$$

Length scales based on integral definitions are less sensitive to errors. Fig. 12 shows the boundary-layer displacement thickness

$$\delta_1 = \int_0^\infty \left(1 - \frac{\langle u\rangle}{U_\delta}\right) \mathrm{d}y, \tag{12}$$

the boundary-layer momentum thickness

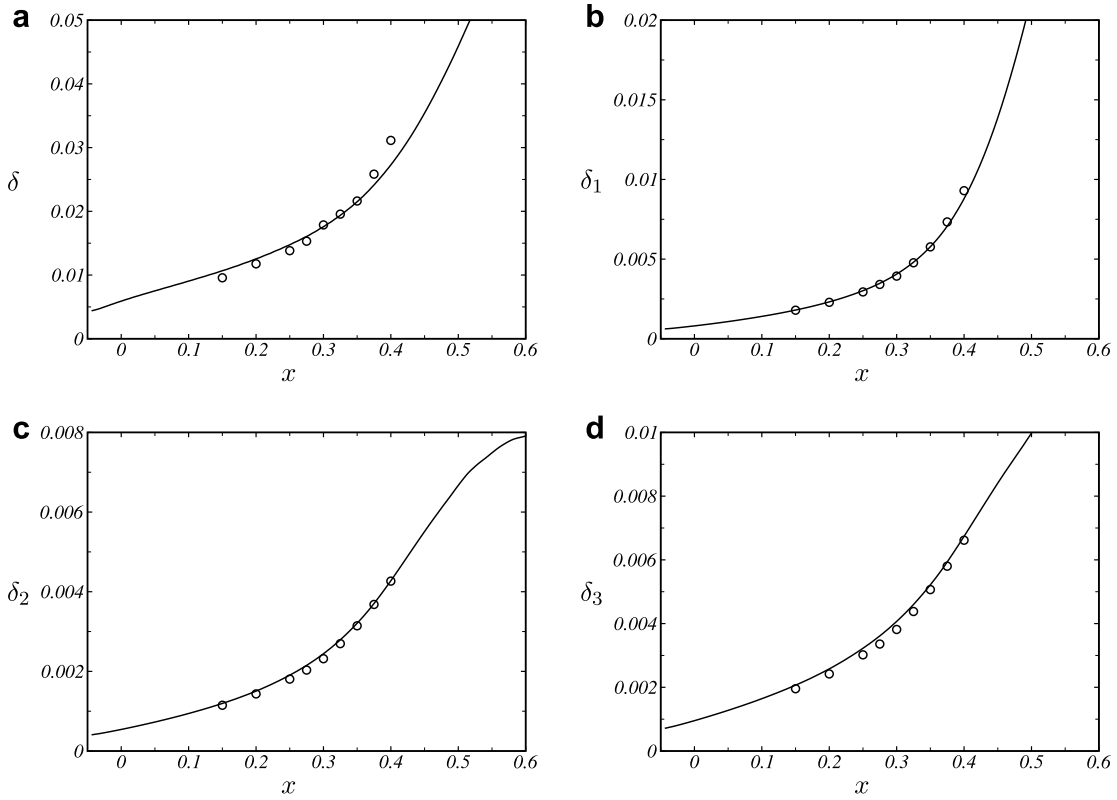

Fig. 12. Integral measures for the boundary-layer thickness: (a) boundary-layer thickness, (b) displacement thickness, (c) momentum thickness and (d) energy thickness. — LES, ○ measurement.

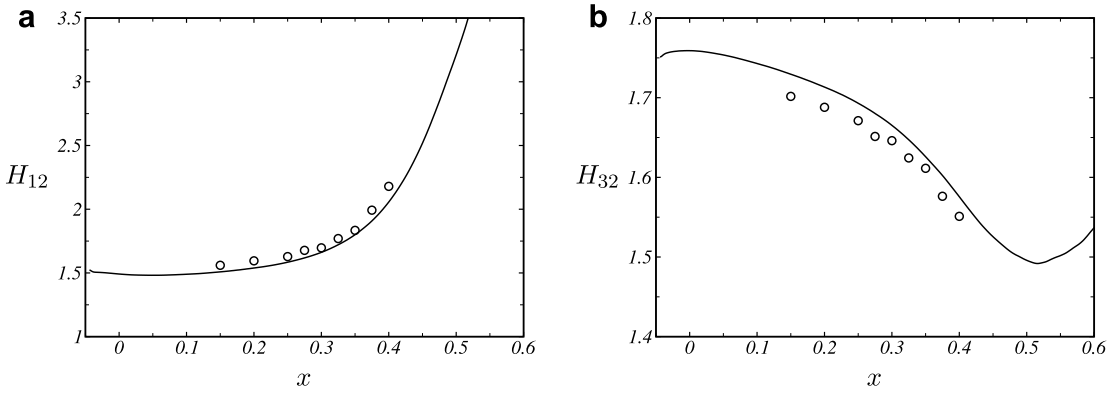

Fig. 13. Shape parameters: (a) H_{12} displacement thickness to momentum-loss thickness and (b) H_{32} energy-loss thickness to momentum-loss thickness. — present LES, ∘ LDA measurement.

Table 6
Characteristic parameters of the adverse-pressure-gradient boundary-layer simulation

x	Re_δ	Re_{δ_1}	Re_{δ_2}	H_{12}	H_{32}	$C_f \times 10^3$	β
0.0	7478	1025	686.9	1.49	1.76	5.285	0.211
0.1	10641	1651	1108.5	1.49	1.74	4.340	0.524
0.2	13487	2491	1618.7	1.54	1.71	3.502	1.308
0.3	16944	3912	2354.6	1.66	1.67	2.477	4.038
0.4	23156	7463	3628.8	2.06	1.58	0.997	20.85
0.5	35212	16427	5115.5	3.21	1.50	0.009	3456.
0.6	50668	29550	5699.2	5.18	1.54	-0.160	226.3

$$\delta_2 = \int_0^\infty \frac{\langle u\rangle}{U_\delta}\left(1 - \frac{\langle u\rangle}{U_\delta}\right)\mathrm{d}y, \tag{13}$$

and the boundary-layer energy thickness

$$\delta_3 = \int_0^\infty \frac{\langle u\rangle}{U_\delta}\left(1 - \left(\frac{\langle u\rangle}{U_\delta}\right)^2\right)\mathrm{d}y. \tag{14}$$

Pressure gradient and incipient separation result in a fast growth of the boundary-layer thicknesses. We observe a very good agreement between experiment and simulation for δ_1, δ_2, and δ_3, see Fig. 12.

The different thickness measures are used to define non-dimensional parameters which characterize the shape variation of the mean velocity profile. The parameters H_{12} and H_{32}, see Fig. 13, are defined as the ratio of displacement thickness to momentum thickness

$$H_{12} = \frac{\delta_1}{\delta_2}, \tag{15}$$

and as the ratio of energy thickness to momentum thickness

$$H_{32} = \frac{\delta_3}{\delta_2}, \tag{16}$$

respectively. Near the inflow, H_{12} is approximately 1.5. The parameter H_{12} increases with incipient backflow and doubles its value before boundary-layer separation. H_{32} shows a notable inflow transient, that might result from the fact that the pressure gradient adjusts rapidly behind the inflow boundary. After this transient, H_{32} decreases from about 1.75 to a minimum of about 1.5 at detachment, see Table 6. Simulation and experiment show essentially the same behavior, where the LES predicts slightly higher values for H_{32} and slightly lower values for H_{12} than those determined experimentally.

The viscous length scale $l^+ = \nu/U_\tau$ characterizes the size of the smallest coherent structures that occur close to the wall. An integral scale based on a defect formulation and the wall-friction velocity is the Rotta-Clauser length

$$\Delta_{RC} = \int_0^\infty \frac{U_\delta - \langle u\rangle}{U_\tau}\mathrm{d}y. \tag{17}$$

Graphs for both length scales are presented in Fig. 14 showing a good agreement between LES and experiment. Differences between LES and experiment can be attributed to the Preston-tube measurement of U_τ which will be discussed in the following section.

From the characteristic scales of the boundary layer various non-dimensional Reynolds numbers can be computed. Fig. 15 shows the displacement-thickness Reynolds number Re_{δ_1} and the momentum-thickness Reynolds number Re_{δ_2} for experiment and computation, which are in good agreement.

6.4. Pressure-gradient parameters

Dimensionless pressure-gradient parameters are frequently used to classify and to compare APG boundary-layer flows. Fig. 16 shows four widely used parameters, namely the Clauser pressure parameter (Clauser, 1954)

$$\beta = \frac{\delta_1}{\rho U_\tau^2}\langle \partial_x p\rangle, \tag{18}$$

the Patel pressure gradient (Patel, 1965)

$$\Delta_P = \frac{\nu}{\rho U_\tau^3}\langle \partial_x p\rangle, \tag{19}$$

the pressure-gradient parameter of Castillo et al. (Castillo and George, 2001; Castillo et al., 2004)

$$\Lambda_{\delta_2} = \frac{\delta_2}{\rho U_\delta^2 \partial_x \delta_2}\langle \partial_x p\rangle, \tag{20}$$

and the acceleration parameter

$$K = \frac{\nu}{U_\delta^2}\langle \partial_x U_\delta\rangle. \tag{21}$$

The latter parameter has the advantage that it does not incorporate the pressure gradient and the wall-shear stress. By Bernoulli's equation its link to the pressure gradient is

$$K = -\frac{\nu}{\rho\, U_\delta^3}\langle \partial_x p_\delta\rangle. \tag{22}$$

Clauser (1954) proposed $\beta = const$ as criterion for determining the equilibrium similarity state of boundary layers with pressure gradient. The pressure-gradient parameter Δ_P was used by Patel (1965) for grading the severity of the pressure gradient as it affects Preston-tube measurements. In a more recent analysis, Castillo and George (2001) argued that rather a constant value of the pressure parameter

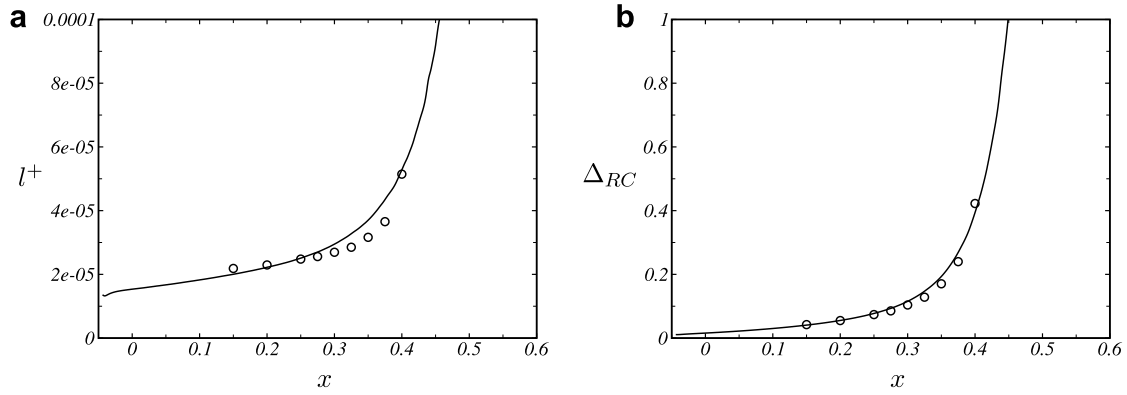

Fig. 14. Length scales based on wall-friction for — present LES and for ◦ Indinger's Preston-tube measurement. (a) viscous length-scale. (b) Rotta-Clauser length.

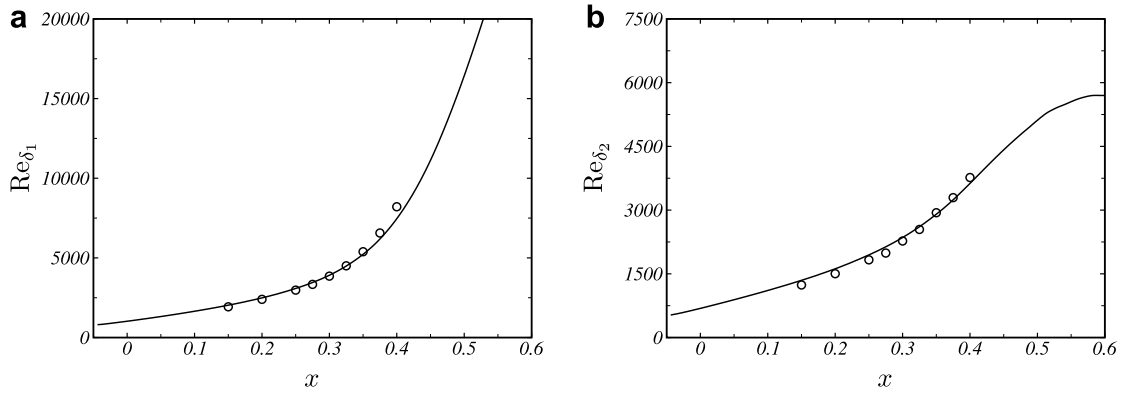

Fig. 15. (a) Reynolds number based on momentum-loss thickness and (b) Reynolds number based on displacement thickness, and — present LES and ◦ LDA measurement.

$$\Lambda = \frac{\delta}{\rho U_\delta^2 \partial_x \delta} \langle \partial_x p \rangle, \tag{23}$$

is the necessary condition for equilibrium. Castillo et al. (2004) found that $\Lambda_{\delta_2} \approx \Lambda$ has nearly the same value, $\Lambda_{\delta_2} = 0.21 \pm 0.01$, for most APG equilibrium boundary layers and that even separating boundary layers have a tendency to remain in an equilibrium state. Following this result, most experimentally studied boundary layers are equilibrium boundary layers. The boundary layer flow investigated in this work is in strong non-equilibrium state under both the β criterion and the Λ_{δ_2} criterion. The parameter values computed from the LES and the experimental data agree well, see Fig. 16.

The characteristic velocity of the near-wall region is the wall-friction velocity $U_\tau = \sqrt{\nu |\langle \partial_y u \rangle|_{\text{wall}}}$. Fig. 17a shows the experimental wall-friction velocity and that of the present LES. Some differences between LES and experiment are evident and become more visible for the local non-dimensional wall-friction coefficient $C_f = 2U_\tau^2/U_\delta^2$, see Fig. 17b. We believe that these differences result mostly from uncertainties in the experimental determination of the wall friction.[1] Indinger used a Preston tube to measure the dynamic pressure at the wall from which the wall-friction velocity U_τ was computed by means of tabulated calibration data of Head and Ram (1971). By construction, Preston-tube measurements are inaccurate for flow regions with instantaneous backflow, i.e. from ID onwards. Even for attached flow the accuracy is limited under the presence of strong pressure gradients (Patel, 1965).

[1] Indinger, personal communication.

This issue is now investigated more closely by using another means of computing C_f from experimental data. Following Fernholz (1964), the empirical formula

$$C_f = 0.058 \ \lg\left(\left(\frac{8.05}{H_{12}}\right)^{1.818}\right)^{1.705} Re_{\delta_2}^{-0.268} \tag{24}$$

allows to approximate the local wall-friction coefficient from the non-dimensional integral parameters H_{12} (15) and Re_{δ_2} (2) which are less sensitive to measurement errors. In Fig. 17b this correlation is applied to both the experimental and the numerical data. A good agreement of the simulation with the experiment is observed. In the region with significant backflow, between ID and D, the correlation functional of Fernholz (1964) gives C_f almost identical to that computed from the wall-friction of the LES.

6.5. Turbulent fluctuations

In addition to mean-velocity profiles, Indinger (2005) provides second-order correlations of the streamwise velocity. LES and experiment compare well for the r.m.s. fluctuation of the streamwise velocity component, see Fig. 19. With decreasing distance from the separation a characteristic change of the shape of the fluctuation profiles is observed. The stress' maximum associated with the buffer layer weakens and a new maximum is formed in the outer part. Contours of the turbulent kinetic energy and the Reynolds shear stress for the LES prediction are shown in Fig. 18.

Both the simulation and the experiment show the same qualitative profiles and tendencies. After a perfect quantitative match at the first stations the experimental fluctuations are slightly lower than the prediction at the later stations. Note that this finding is

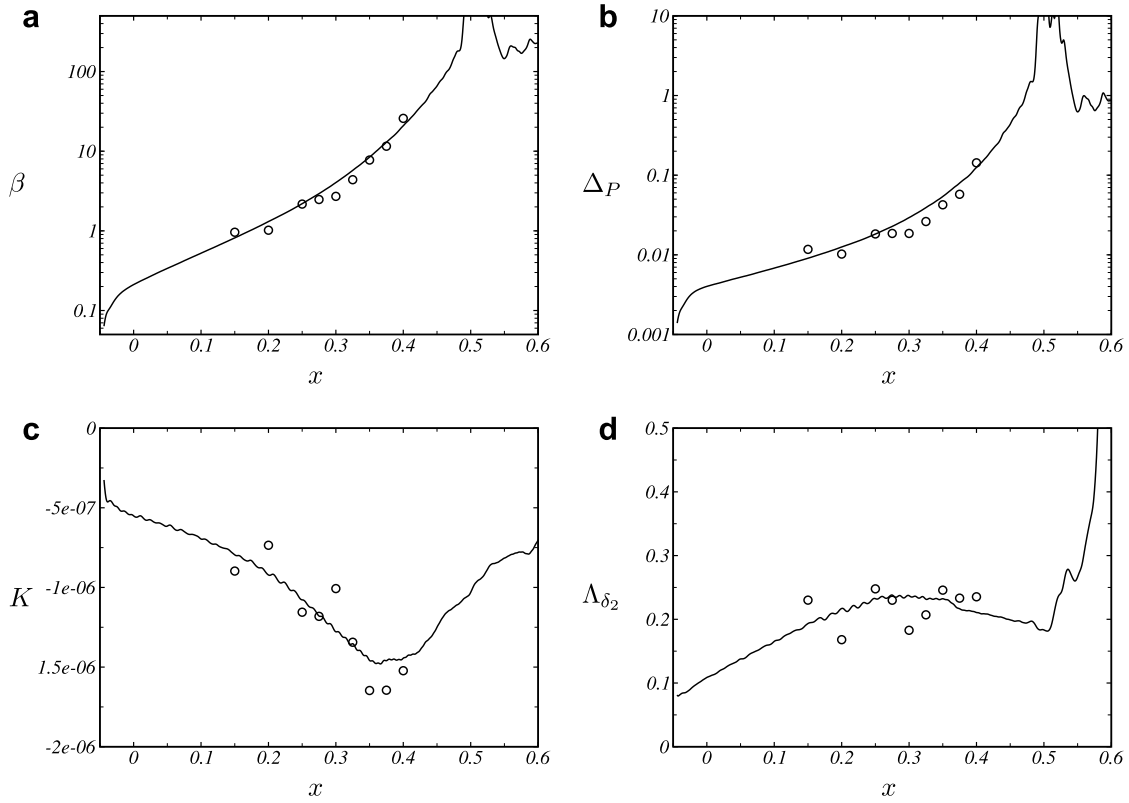

Fig. 16. Pressure-gradient parameters (a) Clauser pressure-gradient parameter, (b) Patel pressure gradient, (c) dimensionless pressure-gradient parameter K and (d) dimensionless pressure-gradient parameter Λ_{δ_2}. — present LES, ○ experiment.

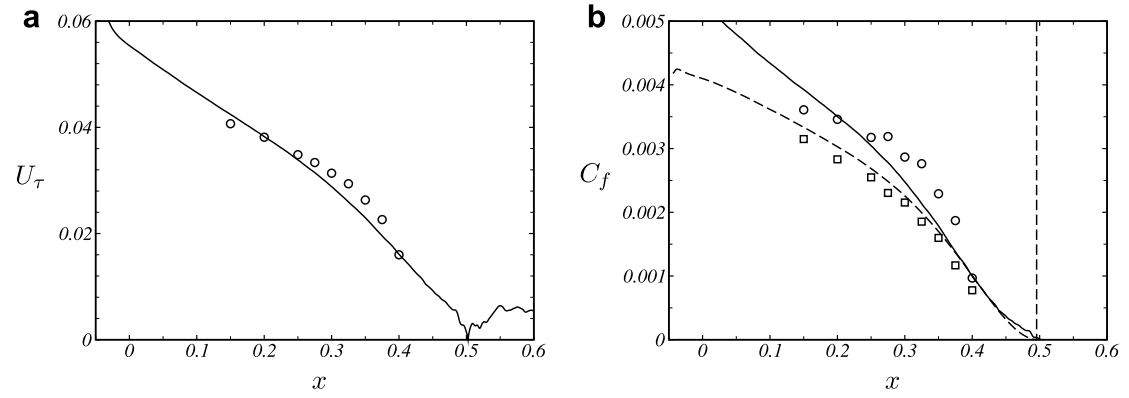

Fig. 17. (a) Wall-friction velocity U_τ — present LES, ○ Preston-tube measurement. (b) Local wall-friction parameter C_f — from present LES, ○ Preston-tube measurement, - - - - correlation of Fernholz (1964) using LES data, □ correlation of Fernholz (1964) using LDA measurements.

consistent with the fact that not only the LES but also the measured data are filtered. Indinger (2005, p. 182) states 5.6×10^{-4} for the spanwise extent of the LDA system's measurement volume, which corresponds to twice the LES filter width. Additional smoothing operations are involved in the analysis of the LDA data. It remains an open question whether the experimental or the numerical data is closer to the physical fluctuations which are unknown.

6.6. Separation dynamics

The separated-flow region reflects the turbulent nature of the incoming boundary layer and shows a rather complex behavior. A flow visualization is presented in Fig. 20. In front of the large separated zone, small zones of reverse flow are continuously formed which then either move slowly downstream and join the separated region or disappear shortly after their appearance. This highly active zone ranges from $x = 0.4$ to $x = 0.55$. We have observed that the separated zone can be divided into two subregions that move independently. Also typical for this configuration is secondary flow separation which occurs inside large separated regions.

Fig. 21 shows contours of the instantaneous streamwise wall-shear stress. Different regimes of wall turbulence can be distinguished. Typical streaks dominate the boundary layer at the inflow. As the flow experiences the adverse pressure gradient, the average width of the streaks grows and their relative length decreases. Intermittent backflow is observed from

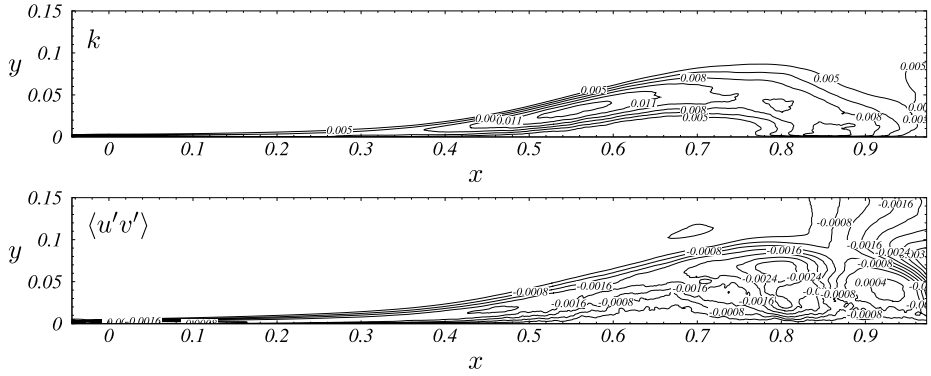

Fig. 18. Contours of turbulence energy and mean Reynolds shear stress.

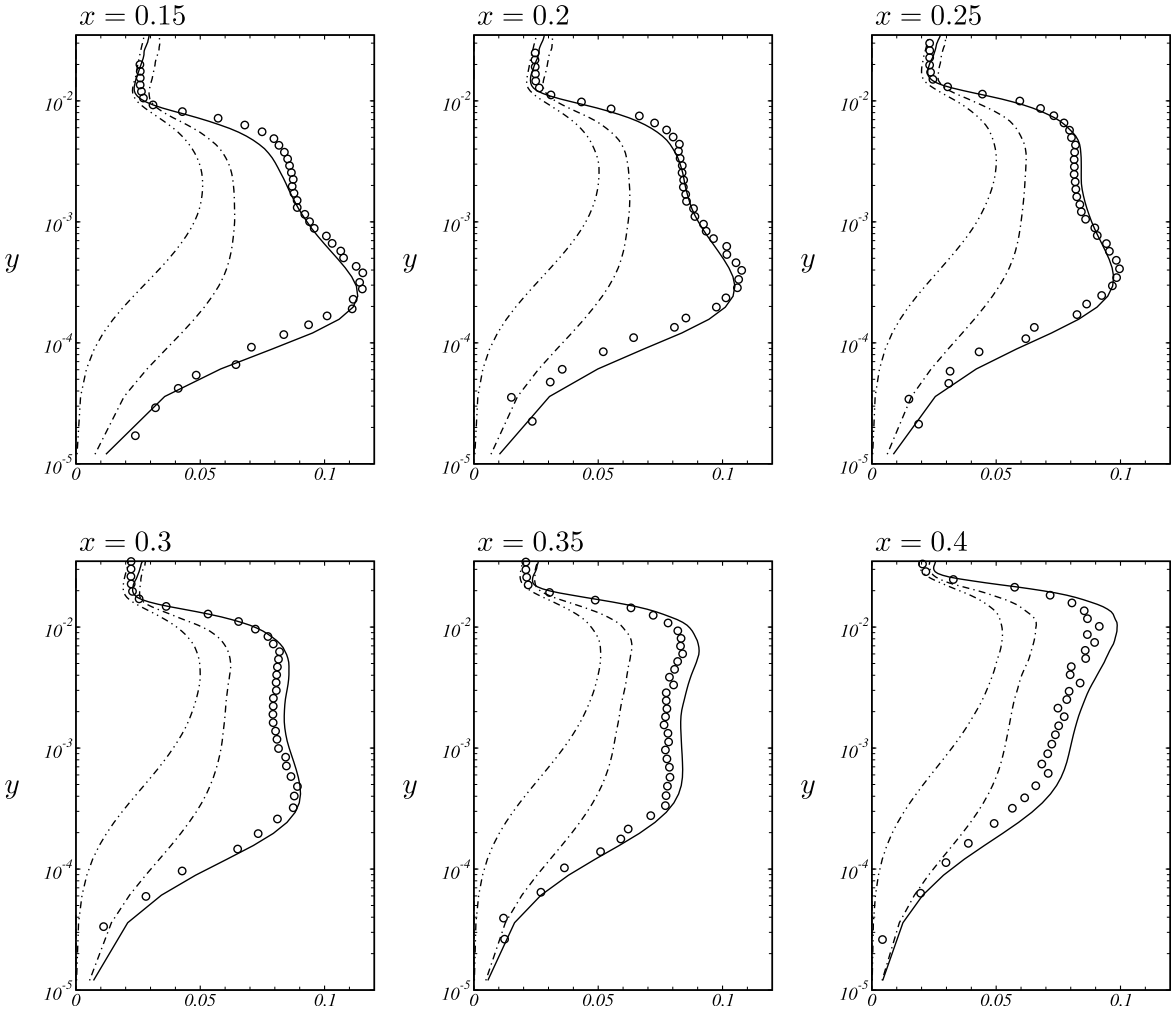

Fig. 19. Profiles of velocity fluctuations for several downstream stations. — $\langle u'u' \rangle^{1/2}$, -..-..- $\langle v'v' \rangle^{1/2}$, and .-.-.- $\langle w'w' \rangle^{1/2}$ for LES, ○ for LDA.

$x = 0.1$ onwards. There is no well-defined separation line, instead the fraction of separated flow zones increases gradually. Energetic streak-like structures can penetrate deeply into the detached region. Within the separated region eddies with large spanwise extents are dominating. Secondary flow reversion occurs in several regions. Streaky structures are found again at the reattachment. The reattachment line is much smoother than the detachment line. Generally, the flow structures observed at and after reattachment are one order of magnitude larger than those within the attached boundary layer before separation.

7. Conclusions

Large-eddy simulations of incompressible flat-plate boundary-layer flows were conducted. The effect of subgrid-scales is modeled by the adaptive local deconvolution method (ALDM). ALDM represents a full merger of SGS model and discretization scheme. Model parameters were previously determined by a spectral analysis of the effective eddy viscosity in isotropic turbulence in the Reynolds number's infinite limit and were used for the computations in this paper without adjustments. Computational results presented in

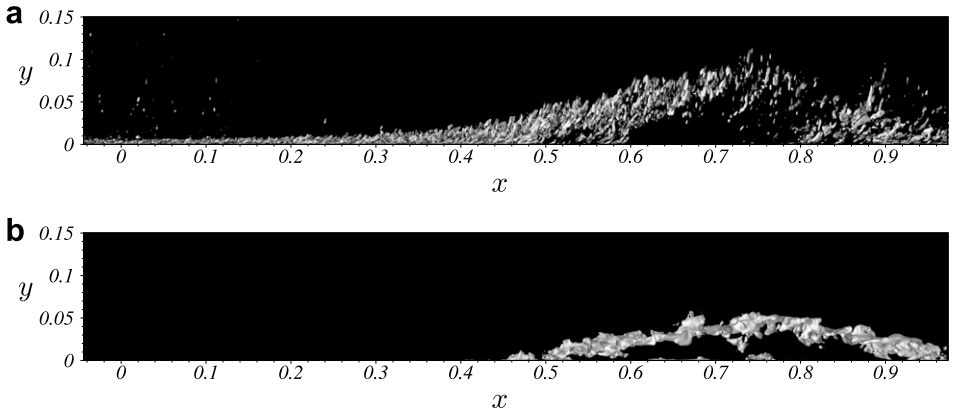

Fig. 20. Instantaneous snapshot of: (a) vortical structures visualized by iso-surfaces of the Q criterion and (b) flow separation visualized by the iso-surface of zero streamwise velocity.

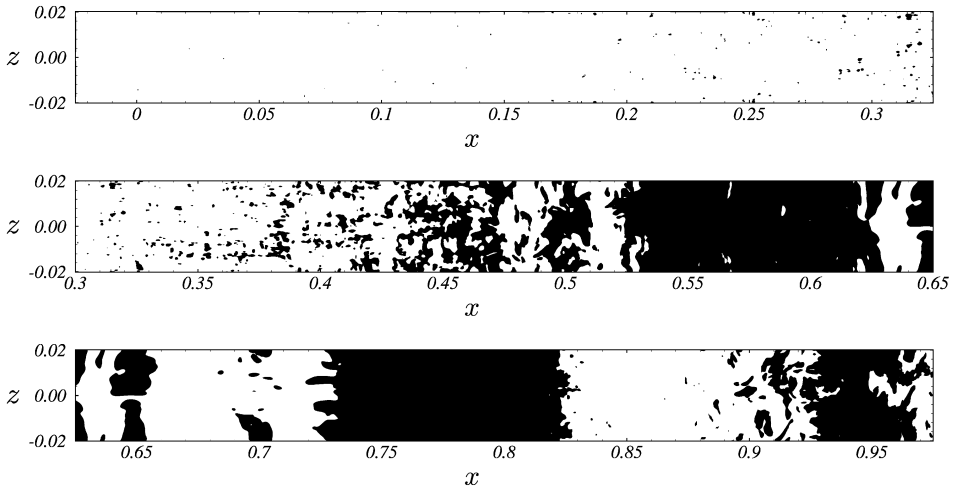

Fig. 21. Instantaneous contours of negative streamwise wall-shear stress.

this paper provide evidence for the novel subgrid-scale model's validity in physically complex wall-bounded flows.

First, transition from laminar flow to turbulence in a Blasius boundary layer was considered. The evolution of integral flow parameters is in excellent agreement with theory and empirical correlations. In the turbulent regime the performance of the SGS model was evaluated by comparing profiles of mean velocity and Reynolds stresses with DNS data. Results from implicit LES agree well with the DNS reference. ALDM predicts the anisotropic turbulence statistics correctly.

Secondly, well resolved large-eddy simulations of a fully turbulent flat-plate boundary-layer flow subjected to a constant adverse pressure gradient (APG) were presented. Reynolds number and pressure-gradient parameters were adapted to the experimental setup of Indinger. Under the conditions considered here the adverse pressure gradient leads to a highly unsteady and massive separation. Neither separation nor reattachment are fixed in space. The computational results were validated against the experimental data. Experiment and LES agree very well thus providing a final validation of the implicit SGS modeling framework provided by ALDM. To improve the understanding of wall-bounded turbulence in the vicinity of massive pressure-induced separation, a deeper analysis of the computational results is planned for the future.

Acknowledgements

Dr. Indinger is gratefully acknowledged for providing his experimental data and for many helpful discussions. This work has been partially supported under the WALLTURB project. WALLTURB (A European synergy for the assessment of wall turbulence) is funded by the CEC under the 6th framework program (contract AST4-CT-2005-516008). Financial support has also been provided by the German Research Council (Deutsche Forschungsgemeinschaft – DFG) in the framework of the French-German research group FG507. Computational resources have been provided by the Stuttgart High-Performance Computing Center (HLRS).

References

Castillo, L., George, W.K., 2001. Similarity analysis for turbulent boundary layer with pressure gradient: outerflow. AIAA J. 39 (1), 41–47.

Castillo, L., Wang, Xia, George, W.K., 2004. Separation criterion for turbulent boundary layers via similarity analysis. J. Fluids Eng. 126 (1), 297–303.

Clauser, F.H., 1954. Turbulent boundary layers in adverse pressure gradient. J. Aeronaut. Sci. 21, 91–108.

Domaradzki, J.A., Radhakrishnan, S., 2005. Eddy viscosities in implicit large eddy simulations of decaying high Reynolds number turbulence with and without rotation. Fluid Dynam. Res. 36, 385–406.

Fernholz, H.-H., 1964. Halbempirische Gesetze zur Berechnung turbulenter Grenzschichten nach der Methode der Integralbedingungen. Ingenieur-Archiv 33 (6), 384–395.

Grinstein, F., Margolin, L., Rider, W. (Eds.), 2007. Implicit Large Eddy Simulation: Computing Turbulent Flow Dynamics. Cambridge University Press, Cambridge, UK.

Head, M.R., Ram, V.V., 1971. Improved presentation of preston tube calibration. Aeronaut. Quat. 22, 295–300.

Hickel, S., Adams, N.A., 2006. Efficient implementation of nonlinear deconvolution methods for implicit large-eddy simulation. In: Nagel, W., Jäger, W., Resch, M. (Eds.), High Performance Computing in Science and Engineering. Transactions of the High Performance Computing Center, Stuttgart (HLRS). Springer, pp. 293–306.

Hickel, S., Adams, N.A., 2007. On implicit subgrid-scale modeling in wall-bounded flows. Phys. Fluids 19, 105106.
Hickel, S., Adams, N.A., Domaradzki, J.A., 2006. An adaptive local deconvolution method for implicit LES. J. Comp. Phys. 213, 413–436.
Hickel, S., Adams, N.A., Mansour, N.N., 2007. Implicit subgrid-scale modeling for large-eddy simulation of passive-scalar mixing. Phys. Fluids 19, 095102.
Hickel, S., T. Kempe, and N.A. Adams (2007). Implicit large-eddy simulation applied to turbulent channel flow with periodic constrictions. Theoret. Comput. Fluid Dynamics, in press. doi:10.1007/s00162-007-0069-7.
Indinger, T. (2005). Einfluss eines positiven Druckgradienten auf turbulente Grenzschichten an glatten und gerillten Oberflächen. Ph. D. thesis, TU München.
Indinger, T., Buschmann, M.H., Gad-el-Hak, M., 2006. Mean-velocity profile of turbulent boundary layers approaching separation. AIAA J. 44 (11), 2465–2474.
Indinger, T., Hickel, S., Adams, N., 2004. 3d-measurements in an adverse-pressure-gradient turbulent boundary layer over smooth and ribbed surfaces. In: Proceedings of the 21st International Congress of Theoretical and Applied Mechanics (ICTAM), Warsaw, Poland.
Kalter, M., Fernholz, H.H., 2001. The reduction and elimination of a closed separation region by free-stream turbulence. J. Fluid Mech. 446, 271–308.
Lund, T., Wu, X., Squires, K., 1998. Generation of turbulent inflow data for spatially-developing boundary layer simulations. J. Comp. Phys. 140, 233–258.
Manhart, M., Friedrich, R., 2002. DNS of a turbulent boundary layer with separation. Int. J. Heat Fluid Flow 23, 572–581.
Morinishi, Y., Lund, T., Vasilyev, O., Moin, P., 1998. Fully conservative higher order finite difference schemes for incompressible flow. J. Comput. Phys. 143, 90–124.
Na, Y., Moin, P., 1998a. Direct numerical simulation of a separated turbulent boundary layer. J. Fluid Mech. 374, 379–405.
Na, Y., Moin, P., 1998b. The structure of wall-pressure fluctuations in turbulent boundary layers with adverse pressure gradient and separation. J. Fluid Mech. 377, 347–373.
Patel, V.C., 1965. Calibration of the Preston tube and limitations on its use in pressure gradients. J. Fluid Mech. 23 (1), 185–208.
Schlichting, H., 1979. McGraw-Hill.
Shu, C.-W., 1988. Total-variation-diminishing time discretizations. SIAM J. Sci. Stat. Comput. 9 (6), 1073–1084.
Simpson, R.L., 1981. A review of some phenomena in turbulent flow separation. J. Fluids Eng. 102, 520–533.
Simpson, R.L., 1989. Turbulent boundary-layer separation. Annu. Rev. Fluid Mech. 21, 205–234.
Spalart, P.R., 1988. Direct simulation of a turbulent boundary layer up to $Re_\theta = 1410$. J. Fluid Mech. 187, 61–98.
Spalart, P.R., Coleman, G.N., 1997. Numerical study of a separation bubble with heat transfer. Eur. J. Mech. B Fluids 16, 169–189.
van der Vorst, H., 1992. Bi-CGSTAB: A fast and smoothly converging variant of Bi-CG for the solution of nonsymmetric linear systems. SIAM J. Sci. Statist. Comput. 13, 631–644.